J. Fluid Mech. (2008), *vol.* 604, *pp.* 389–409. © 2008 Cambridge University Press
doi:10.1017/S0022112008001328 Printed in the United Kingdom

Dynamics and mixing of vortex rings in crossflow

RAJES SAU AND KRISHNAN MAHESH
Aerospace Engineering & Mechanics, University of Minnesota, Minneapolis, MN 55455, USA

(Received 12 September 2007 and in revised form 26 February 2008)

Direct numerical simulation is used to study the effect of crossflow on the dynamics, entrainment and mixing characteristics of vortex rings issuing from a circular nozzle. Three distinct regimes exist, depending on the velocity ratio (ratio of the average nozzle exit velocity to free-stream crossflow velocity) and stroke ratio (ratio of stroke length to nozzle exit diameter). Coherent vortex rings are not obtained at velocity ratios below approximately 2. At these low velocity ratios, the vorticity in the crossflow boundary layer inhibits roll-up of the nozzle boundary layer at the leading edge. As a result, a hairpin vortex forms instead of a vortex ring. For large stroke ratios and velocity ratio below 2, a series of hairpin vortices is shed downstream. The shedding is quite periodic for very low Reynolds numbers. For velocity ratios above 2, two regimes are obtained depending upon the stroke ratio. Lower stroke ratios yield a coherent asymmetric vortex ring, while higher stroke ratios yield an asymmetric vortex ring accompanied by a trailing column of vorticity. These two regimes are separated by a transition stroke ratio whose value decreases with decreasing velocity ratio. For very high values of the velocity ratio, the transition stroke ratio approaches the 'formation number'. In the absence of trailing vorticity, the vortex ring tilts towards the upstream direction, while the presence of a trailing column causes it to tilt downstream. This behaviour is explained. In the absence of crossflow, the trailing column is not very effective at entrainment, and is best avoided for optimal mixing and entrainment. However, in the presence of crossflow, the trailing column is found to contribute significantly to the overall mixing and entrainment. The trailing column interacts with the crossflow to generate a region of high pressure downstream of the nozzle that drives crossflow fluid towards the vortex ring. There is an optimal length of the trailing column for maximum downstream entrainment. A classification map which categorizes the different regimes is developed.

1. Introduction

Jets in crossflow are central to a variety of important applications such as dilution holes in combustors, fuel injectors, pollutant dispersion from smoke stacks, thrust vectoring of turbojets, and V/STOL aircraft. There is therefore considerable incentive to actively control jets in crossflow. This paper is motivated by experimental observations on the use of pulsing to control the mixing characteristics of jets in crossflow (e.g. Wu, Vakili & Yu 1988; Chang & Vakili 1995; Eroglu & Briedenthal 2001; Blossey, Narayanan & Bewley 2001; M'Closkey *et al.* 2002; Karagozian; Cortelezi & Soldati 2003). It is observed that pulsing the jet results in the formation of vortex rings whose strength and spacing depend on the frequency and duty cycle of the jet, for a given jet and crossflow combination (Eroglu & Briedenthal 2001). The resulting flow appears to improve mixing rate and increase the entrainment. Some workers (e.g. M'Closkey *et al.* 2002; Shapiro *et al.* 2006) relate the optimal pulse width for maximum penetration of vortical structures, to the 'formation number' proposed

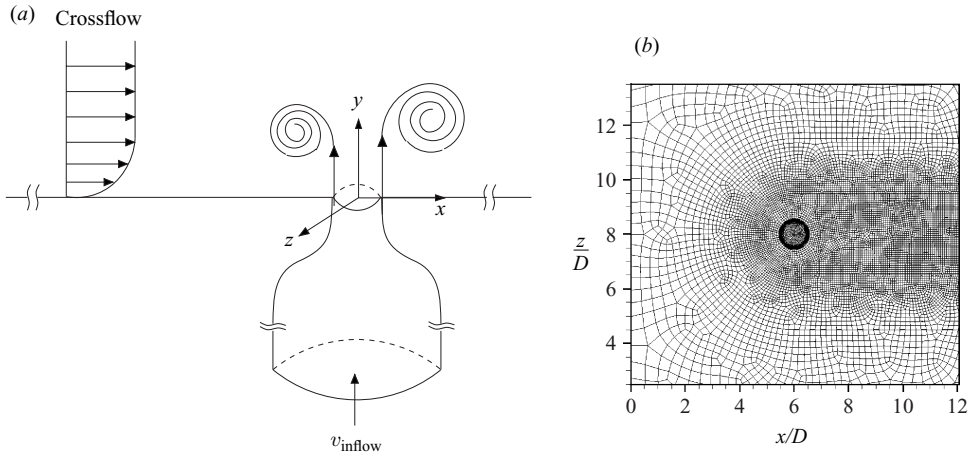

FIGURE 1. (a) Schematic of the problem. (b) Horizontal slice of the mesh.

by Gharib, Rambod & Shariff (1998). Johari (2006) presents scaling arguments, based on the motion of individual vortex rings in stationary fluid, for the penetration and mixing of pulsed jets in crossflow. He proposes classification schemes using the formation number and stroke ratio obtained from the frequency and duty cycle of the pulsed jet.

Sau & Mahesh (2007) used DNS to study optimal mixing by a single vortex ring in stationary fluid. They considered two Schmidt numbers and a range of stroke ratios. The formation number was found to yield the maximum entrainment for both Schmidt numbers. This behaviour was explained by noting that the entrainment was a combination of that due to the leading vortex ring, and that due to the trailing column of vorticity. The entrainment by the trailing column was negligible compared to that by the vortex ring, as a result of which the relative contribution of the vortex ring to overall entrainment decreases beyond the formation number.

The above study ignores the effect of crossflow. This paper therefore studies the effect of crossflow on the dynamics, mixing and entrainment characteristics of vortex rings. The paper is organized as follows. Section 2 discusses the problem and details of the simulations. The effect of crossflow on ring dynamics is discussed in § 3. The case of very low velocity ratio is presented in § 3.2. Entrainment characteristics of vortex rings and hairpin vortices are presented in § 4. The paper concludes with a classification map of the different flow regimes in § 5.

2. Simulation details

2.1. *Problem statement*

Figure 1(a) shows a schematic of the problem, in which a slug of fluid is pushed through a cylindrical nozzle with 3:1 diameter ratio. The nozzle fluid forms a vortex ring as it exits the nozzle. The vortex ring interacts with the crossflow which is directed along the x-direction. The crossflow is modelled as a laminar boundary layer over a flat plate. Note that the origin of the coordinate system is located at the centre of the nozzle exit plane, and the nozzle axis points in the y-direction.

In experiments, vortex rings are often generated by a piston pushing a column of fluid of length L through an orifice of diameter D. In simulations, this process is modelled by specifying a top-hat velocity profile (U_{in}) at the nozzle inflow for a

duration of time τ (referred to as piston time duration). The inflow velocity is zero for time greater than τ. The stroke length and non-dimensional time are determined using the mean nozzle exit velocity, $\overline{U}_{exit}$, which is equivalent to the piston velocity. The stroke length L is therefore equal to $\overline{U}_{exit}\tau$, and the stroke ratio (L/D) is equal to $\overline{U}_{exit}\tau/D$. The stroke ratio is varied by changing the piston time duration τ. The velocity ratio r is defined as the ratio of mean nozzle exit velocity $(\overline{U}_{exit})$ to the free-stream crossflow velocity (u_∞). The velocity ratio is varied by changing the crossflow velocity. DNS of single vortex rings are performed for stroke ratios varying from 1.6 to 8 and crossflow velocity ratios ranging from 1 to 6. The Reynolds number based on $\overline{U}_{exit}$ and nozzle exit diameter (D) is 600 in all cases, except where noted below.

2.2. *Numerical details*

The governing equations are the incompressible Navier–Stokes and continuity equations,

$$\frac{\partial u_i}{\partial t} + \frac{\partial u_i u_j}{\partial x_j} = -\frac{\partial p}{\partial x_i} + \nu \frac{\partial^2 u_i}{\partial x_j x_j}, \quad \frac{\partial u_i}{\partial x_i} = 0, \tag{2.1}$$

and the passive scalar equation

$$\frac{\partial C}{\partial t} + \frac{\partial C u_j}{\partial x_j} = \frac{\nu}{Sc} \frac{\partial^2 C}{\partial x_j x_j}. \tag{2.2}$$

Here u_i, p and ν denote the velocities, pressure and kinematic viscosity respectively. C is the concentration of the scalar. The density of the fluid is assumed constant and is absorbed into the pressure. The numerical scheme used to solve the Navier–Stokes equations is described in detail by Mahesh, Constantinescu & Moin (2004). The algorithm stores the Cartesian velocities and pressure at the centroids of the cells (control volumes), and stores the face-normal velocities at the centroids of the faces. The algorithm is a predictor–corrector scheme which emphasizes discrete energy conservation on unstructured grids. This property makes the algorithm robust at high Reynolds numbers without numerical dissipation. The predictor velocities at the control-volume centroids are obtained using the viscous and the nonlinear terms in equation (2.1); the predictor face-normal velocities are then obtained. The predictor face-normal velocity is then projected so that continuity is discretely satisfied. This yields a Poisson equation for pressure which is solved iteratively using a multigrid approach. The pressure field is used to update the Cartesian control volume-velocities. Implicit time-stepping is performed using a Crank–Nicholson scheme. The algorithm has been validated for a variety of problems over a range of Reynolds numbers (Mahesh *et al.* 2004).

The passive scalar is computed using a predictor–corrector method (Muppidi 2006). The scalar field is first advanced using a second-order central difference scheme. The predicted scalar field is corrected in regions of scalar overshoot using a first-order upwind scheme. This corrector step ensures that locally, the passive scalar concentration is bounded (i.e. $C \in [0, 1]$). The scalar is advanced in time explicitly using the second-order Adams–Bashforth scheme in an inner loop. The fluid emerging from the nozzle exit has $C = 1.0$ and the ambient fluid has $C = 0$.

2.3. *Computational domain and boundary conditions*

The computational domain spans $21D \times 20D \times 16D$ above the nozzle exit in the x-, y- and z-directions respectively, and includes a $10D$ length of nozzle. The computational mesh consists of unstructured hexahedral elements. A grid refinement study was performed on grids containing approximately 2.7×10^6, 3.6×10^6 and 7×10^6 elements.

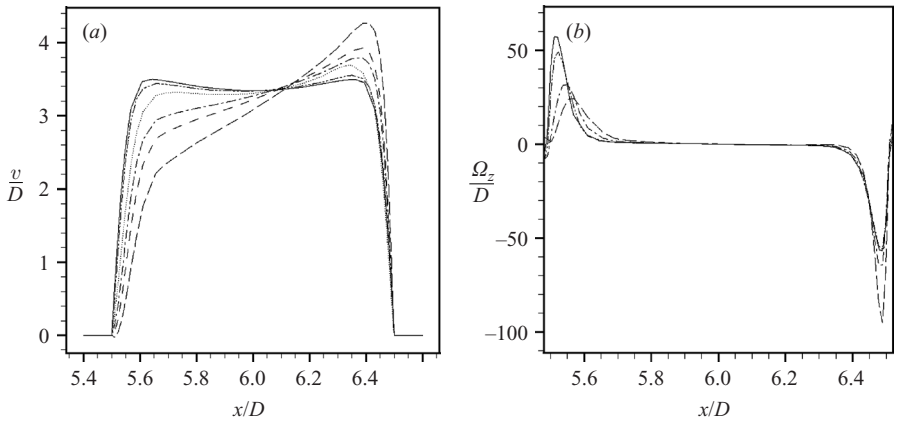

FIGURE 2. (*a*) v-velocity profiles at the nozzle exit in the symmetry plane at $t^* = \overline{U}_{exit}t/D = 1.0$: ——, without crossflow ($r = \infty$); — ·· —, $r = 6$; ·····, $r = 3$; — · —, $r = 2.0$; — — —, $r = 1.5$; — — —, $r = 1.0$. (*b*) Corresponding spanwise vorticity, Ω_z/D profiles: ——, without crossflow ($r = \infty$); — ·· —, $r = 6$; — · —, $r = 2.0$; — — —, $r = 1.0$.

The profiles of nozzle-exit velocity and vorticity for the three grids were examined. The maximum v velocity obtained for the 3.6×10^6 grid differs by 0.6 % from the 2.7×10^6 grid. The 7×10^6 grid deviates less than 0.1% from the 3.6×10^6 grid. The vorticity obtained from the 3.6×10^6 grid deviates less than 0.5% from the 7×10^6 grid. Results from the 7×10^6 grid are presented in the paper. Figure 1(*b*) shows the horizontal cross-section of the mesh (with 3.6×10^6 elements for clarity). Very fine mesh elements are used near the nozzle exit and along the direction of the crossflow. The crossflow is simulated as a laminar flow over a flat plate. The velocity field from the self-similar Blasius boundary layer solution is specified at the inflow plane of the crossflow, $6D$ upstream of the nozzle exit. The velocity field is such that in the absence of nozzle fluid, the crossflow has prescribed $\delta_{50\%}$ at the centre of the nozzle exit. On the spanwise boundaries ($z/D = \pm 8$), the velocity field corresponding to laminar crossflow over a flat plate is prescribed. Free-stream velocity boundary conditions are specified on the top boundary at $y/D = 20$. At the nozzle inflow plane ($y/D = -10$), a top-hat velocity profile is specified:

$$v(x, z, y/D = -10, t) = v_{inflow} = \begin{cases} U_{in} & \text{if } t \leqslant \tau \\ 0 & \text{if } t > \tau. \end{cases}$$

A zero-gradient boundary condition is used at the outflow ($x/D = 24$).

3. Effect of crossflow on ring dynamics

When the ambient fluid is stationary, the shear layer that emerges from the nozzle rolls up into an axisymmetric vortex ring. It propagates away from the nozzle and entrains the ambient fluid radially inwards as it does so. The formation number (Gharib *et al.* 1998) marks the transition between two possible flow structures: vortex ring and vortex ring with trailing column of vorticity. A single vortex ring is produced for stroke ratios less than the formation number, while a vortex ring with trailing column is produced for larger stroke ratios.

Both the formation and propagation of vortex rings are affected by presence of crossflow. The crossflow also breaks the axisymmetry of the ring. Figure 2(*a*) shows

the nozzle exit velocity (v) profiles at the symmetry plane for different velocity ratios at the same instant of time ($t^* = 1.0$). The exit velocity in the absence of the crossflow is also shown. The crossflow momentum decelerates the nozzle fluid on the upstream side ($x/D = 5.5$). As a result of mass conservation, the fluid near the downstream side ($x/D = 6.5$) accelerates as shown in the figure. The peak velocity on the downstream side increases with increasing crossflow velocity. For $r = 1.0$, there is a very small amount of reverse flow at the upstream side of the nozzle. This is because the adverse pressure gradient outside the nozzle exit overcomes the favourable pressure gradient created by the nozzle throat. Profiles of spanwise vorticity at the nozzle exit in the symmetry plane are shown in figure 2(b). Note that vorticity increases significantly on the downstream side due to acceleration of the nozzle fluid. In contrast, the vorticity on the upstream side decreases. Also, the location of peak vorticity on the upstream side shifts to the nozzle right with increasing crossflow velocity. For very low velocity ratios ($r < 2$), the nozzle shear layer at the upstream side does not roll up and a complete vortex ring does not form. The low-velocity-ratio case is discussed in detail in later sections. The following section examines the effect of crossflow on a complete vortex ring. Here, the velocity ratio is greater than 2.

3.1. *Velocity ratio > 2*

For velocity ratio greater than 2, the simulations show that the vortex ring tilts in the presence of crossflow. Tilting is defined in terms of the angle between the plane of the vortex ring and the exit plane of the nozzle. The ring tilts towards the upstream direction for low stroke ratio and tilts towards the downstream for high stroke ratio. This behaviour is discussed in more detail below.

3.1.1. *Low stroke ratio: upstream tilting*

Figure 3 shows contours of Ω_z vorticity in the symmetry plane (x, y) for stroke ratio 2 and velocity ratio 6 at different instants of time. Note that the vortex ring tilts towards the upstream direction as it penetrates into the crossflow. The induced velocity of the vortex ring opposes the crossflow velocity which helps the ring to penetrate deeper into the crossflow. This behaviour is consistent with the experiments of Chang & Vakili (1995), who observed the upstream tilting of vortex rings in low-frequency pulsed jets in crossflow.

The fluid in the vortex ring initially does not have mean horizontal momentum. The relative horizontal velocity between the crossflow and the centroids of the vortex ring combines with ring circulation to produce Kutta–Joukowski lift. It is readily seen that the upstream portion of the ring experiences a downward lift force relative to the downstream portion as shown in figure 4(a). As a result, the ring tilts upstream. Note that this reasoning is two-dimensional at every cross-section of the ring. Two-dimensional simulations of a vortex pair in crossflow were therefore performed to test this hypothesis. The vortex pair was found to tilt upstream as observed here. A quantitative discussion of Kutta–Joukowski lift on vortex cores is provided by Ting & Tung (1965) who consider a vortex core of uniform vorticity embedded in a two-dimensional non-uniform stream. They match the near-field and far-field solutions, and use the Kutta–Joukowski theorem to obtain the resulting force on the vortex. Figures 4(b) and 4(c) show vortex rings of stroke ratio 2 in velocity ratios of 6 and 3. Note that the tilting increases with increase in the crossflow magnitude. This behaviour is consistent with the Kutta–Joukowski lift being responsible for the tilting.

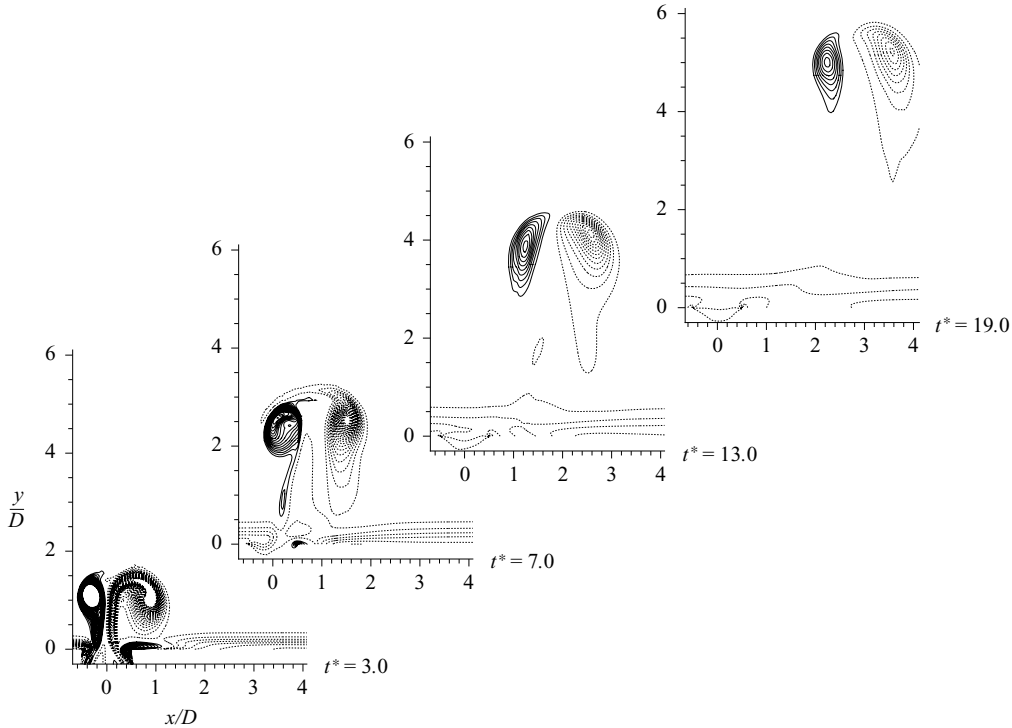

FIGURE 3. Vorticity contours for $L/D = 2$ and $r = 6$ at different time instants. The solid and dashed lines denote positive and negative values respectively.

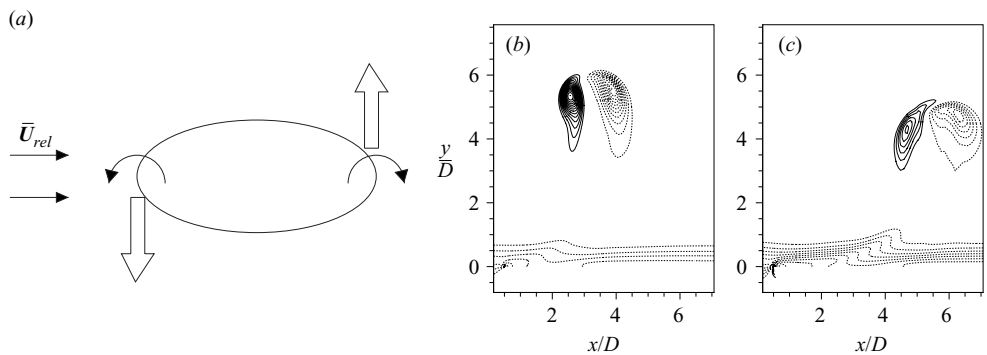

FIGURE 4. (*a*) Schematic of vortex ring tilting. (*b*, *c*) Vorticity contours for $L/D = 2$ at two different crossflow velocities: (*b*) $u_\infty = 0.5$; (*c*) $u_\infty = 1.0$. Note that the tilting increases with increase in the crossflow velocity.

The vortex ring also deforms in the presence of crossflow. The thickness of the ring becomes non-uniform as it propagates into the crossflow. Figure 5(*a*) shows the λ_2 surface of the vortex ring. Note that the downstream side of the ring is thicker than the upstream side. This deformation can be attributed to the strain field experienced by the ring in crossflow. Figure 5(*b*) plots the in-plane velocity magnitude along a curve which encompasses the circumference of the ring from upstream to downstream side on the plane of the ring. The velocity field around the ring suggests that a positive velocity gradient is set up along the ring on the upstream side and a negative velocity

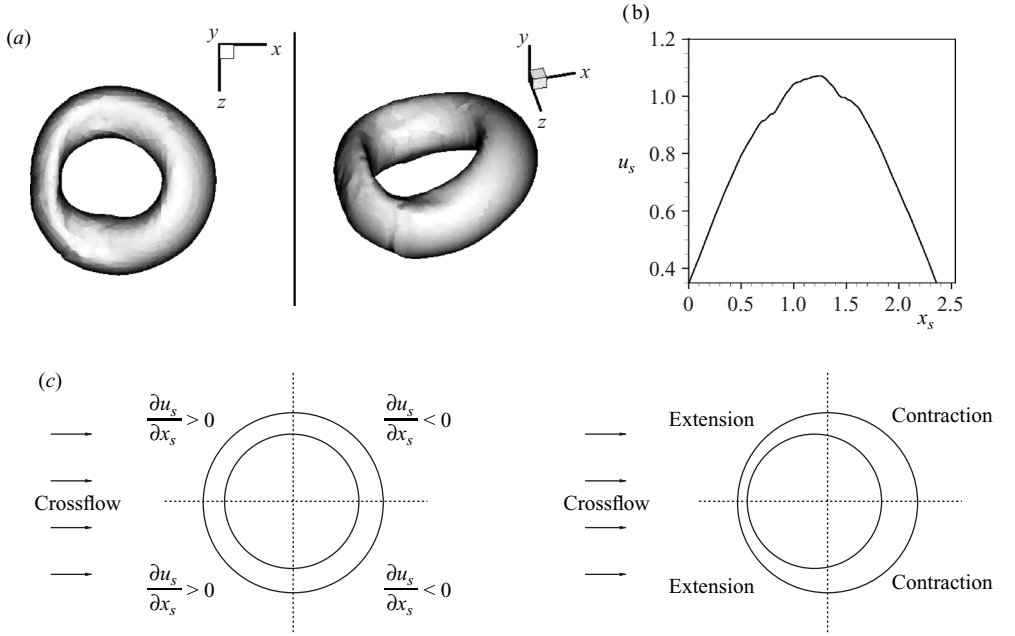

FIGURE 5. (*a*) λ_2-surface of the vortex ring at a distance of around $4D$ from the nozzle exit for L/D of 2 at $r = 3$. (*b*) In-plane velocity magnitude on the circumference of the ring from the upstream to downstream side. (*c*) Schematic to illustrate the velocity gradients along the ring.

gradient is set up along the ring on the downstream side. The corresponding velocity gradients experienced by the ring and the resulting deformation is shown in figure 5(*c*). The upstream side of the ring experiences a positive velocity gradient and stretches as a result. The vortex tube becomes thinner due to stretching. The downstream side exhibits the opposite behaviour.

3.1.2. *High stroke ratio: downstream tilting*

For large stroke ratios, vortex rings along with a trailing column of vorticity are generated. Figure 6 shows the time evolution of Ω_z contours in the symmetry plane for stroke ratio of 6 and velocity ratio of 6. Note that a vortex ring followed by a trailing column is produced. Also, the leading vortex ring tilts towards the downstream direction, unlike its behaviour at lower stroke ratios. One other significant difference is that the ring diameter expands as it propagates downstream (figure 6*b*). This behaviour is due to the enhanced downstream entrainment of crossflow fluid, which is explained later. The ring's induced velocity has a component along the direction of the crossflow which favours downstream movement. The trailing column acts as an obstacle to the crossflow and as a result, the Kutta–Joukowski lift is not produced. Instead, the crossflow bends the leading vortex ring and the trailing column along the direction of the crossflow; finally the leading vortex ring pinches off from the trailing column.

For a fixed velocity ratio, the stroke ratio determines whether the ring tilts upstream or downstream. This suggests that there is a transition stroke ratio which separates these two regimes. So, the transition stroke ratio for $r = 6$ is sought and the effect of crossflow velocity ratio on the transition stroke ratio is examined.

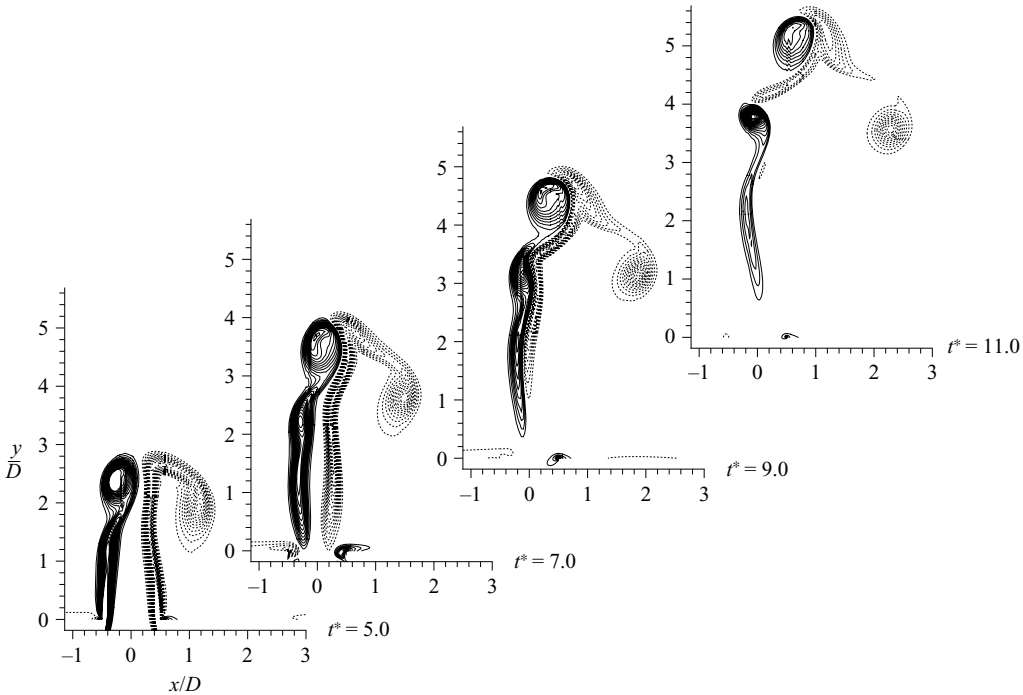

FIGURE 6. Vorticity contours in the symmetry plane for $L/D = 6$ and $r = 6$ at different time instants.

3.1.3. *Transition stroke ratio*

For a fixed crossflow velocity ratio, the transition stroke ratio is obtained from simulations at different stroke ratios. The transition stroke ratio for $r = 6$ is found to be $L/D = 3.3$. The vortex ring tilts in the upstream direction for stroke ratios below 3.3. For stroke ratios larger than 3.3, the vortex ring tilts downstream and the ring diameter expands. The ring dynamics at the transition stroke ratio for $r = 6$ are shown in figure 7. Initially the leading vortex ring tilts in the downstream direction, but eventually it pinches off and tilts in the upstream direction slightly.

The effect of velocity ratio on the transition stroke ratio is examined in figure 8. For $r = 3$, the transition stroke ratio is found to be 2.3; the transition stroke ratio decreases as the velocity ratio decreases. We estimate a 'transition curve' which defines the transition stroke ratio as a function of velocity ratio. Figure 8 shows the three transition stroke ratios obtained at $r = 3$, 4.6 and 6 respectively. The ambient fluid approximates stationary fluid when the velocity ratio is increased to very high values. Recall that in stationary fluid, the 'formation number' ($L/D = 3.6$) defines the transition between single vortex ring and a vortex ring with trailing column. So, the transition curve has an asymptote: $L/D = 3.6$. An exponential curve is fitted which passes through the three data points and has an asymptote at $L/D = 3.6$. This yields the transition stroke ratio $(L/D)_{tr}$ as a function of velocity ratio r:

$$(L/D)_{tr} = F_0 - A_1 \exp(-A_2 r)$$

where $F_0 = 3.6$ denotes the formation number in stationary fluid, and A_1 and A_2 are constants which are obtained as 5.6 and 0.5 respectively. The transition curve is only

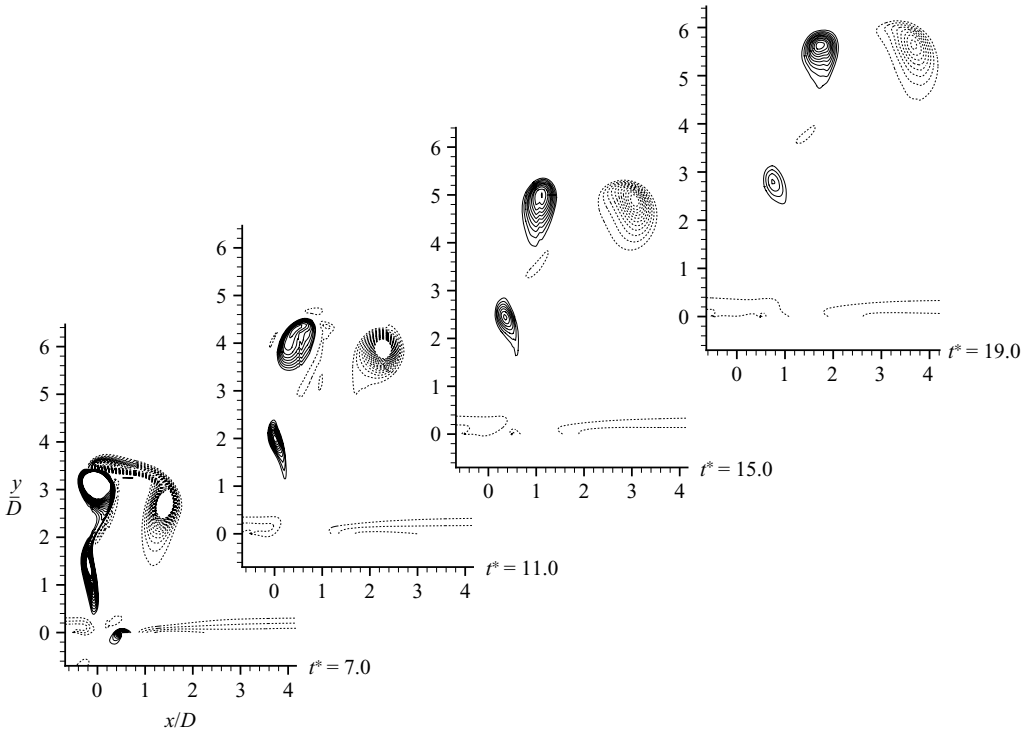

FIGURE 7. Time evolution of vorticity contours at transition stroke ratio ($L/D = 3.33$) for $r = 6$.

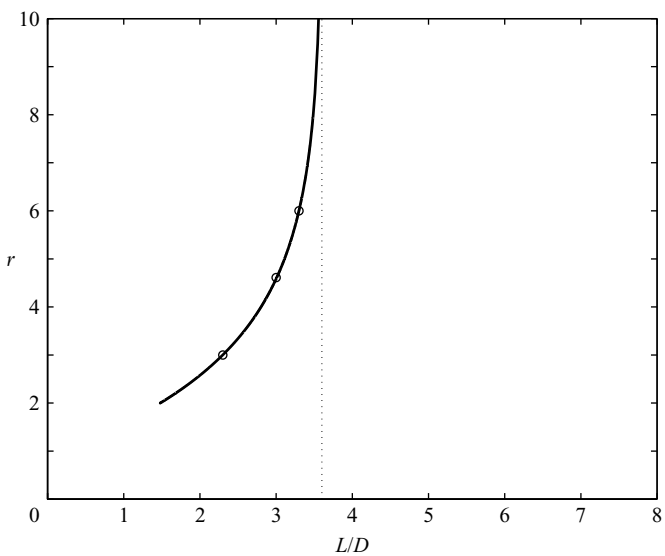

FIGURE 8. The transition curve in the (r, L/D)-plane separates two regimes of flow in the presence of crossflow. The dotted line represents the transition line in stationary flow.

plotted for $r > 2$ as shown in figure 8. It will be shown later that complete vortex rings do not form for $r < 2$.

The transition curve has important practical consequences. For a particular velocity ratio, stroke ratios on the left of the curve shown in figure 8 will generate vortex rings

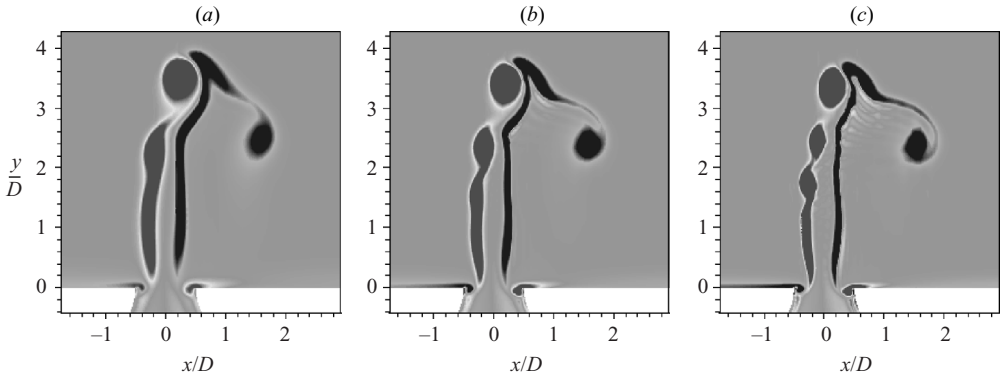

FIGURE 9. Effect of Reynolds number for $L/D = 6$ at $r = 6$: (*a*) $Re = 600$, (*b*) $Re = 900$, (*c*) $Re = 1300$.

which tilt upstream and penetrate into the crossflow. The stroke ratios to the right of this curve will generate rings which tilt downstream and have a trailing column. It will be shown later that the trailing column significantly improves entrainment in crossflow. In terms of penetration of the rings into the crossflow, stroke ratios around the transition curve will provide maximum opposition to the crossflow. For stroke ratios higher than the transition stroke ratio, the ring-tilting will produce a component of the induced momentum along the crossflow and favour downstream movement of the ring. Shapiro *et al.* (2006) performed experiments on a pulsed jet in crossflow and reported maximum penetration at two stroke ratios, one in the range of formation number (3.5–4.7) and the other lying in the range 1.8–2.2. Their jet was acoustically pulsed and r was equal to 2.58. From our results, it can be inferred that the maximum penetration of the pulsed jet is due to the formation of vortex rings which tilt upstream and penetrate deeper into the crossflow. Note that for a velocity ratio $r = 2.58$, the stroke ratio from the transition curve is approximately 2.0 which is in agreement with the experimental observation of Shapiro *et al.* (2006).

The above behaviour is not significantly affected by the Reynolds number, at least in the Reynolds number regime where the rings are stable. Figure 9 shows the vorticity field in the symmetry plane for the vortex ring with $L/D = 6$ and $r = 6$ at three different Reynolds numbers. Note that the Reynolds number has almost no effect on the tilting of the vortex rings. As the Reynolds number increases, the vorticity gradients increase and the instabilities in the trailing jet become more pronounced.

3.2. *Velocity ratio < 2*

The increase in crossflow (i.e. decrease in velocity ratio) causes the vorticity in the crossflow boundary layer to increase. Thus, for very low velocity ratios, the vorticity in the crossflow boundary layer starts interacting with the vorticity of the nozzle boundary layer. The interaction is most significant on the upstream side of the nozzle exit. Figure 10 shows results for three low velocity ratios: 2, 1.5 and 1. Crossflow boundary layer profiles and vorticity contours in the symmetry plane are shown at $t^* = 1.0$ for each case. Note that roll-up of the nozzle boundary layer is inhibited on the upstream side. The vorticity in the emerging boundary layer is cancelled by the opposing vorticity from the crossflow boundary layer. The vorticity cancellation becomes more pronounced as the velocity ratio decreases. For $r = 1.0$, the vorticity in the emerging nozzle boundary layer is almost annihilated by the crossflow boundary layer as shown in figure 10(*c*). So, a complete vortex ring structure does not form. Instead, a hairpin

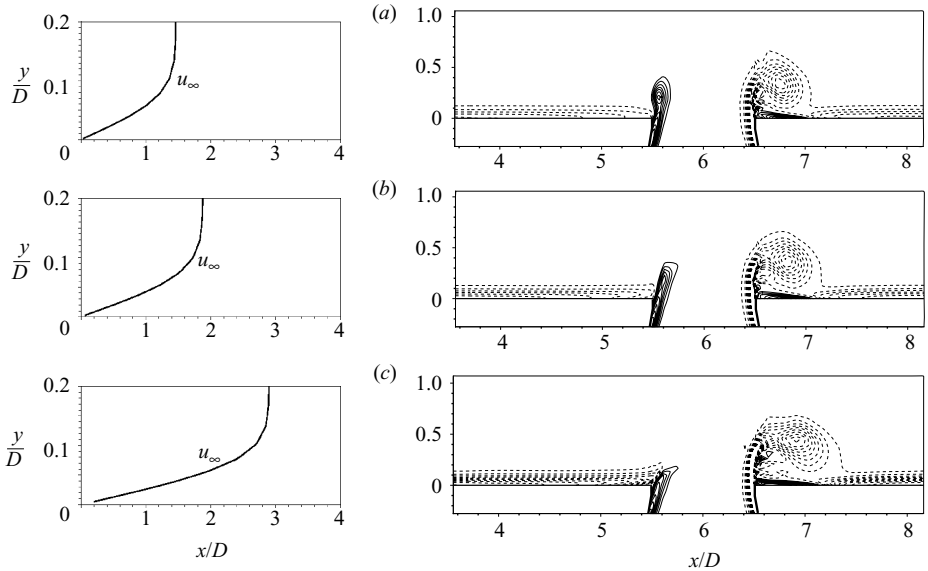

FIGURE 10. Low velocity ratio cases: (*a*) $r = 2.0$, (*b*) $r = 1.5$ and (*c*) $r = 1.0$. Crossflow boundary layer profiles (left) and the vorticity contours in the symmetry plane (right) are shown at $t^* = 1.0$ for each case. Note that the vorticity from the nozzle boundary layers is cancelled by opposing vorticity in the crossflow boundary layer at the upstream side of the nozzle exit.

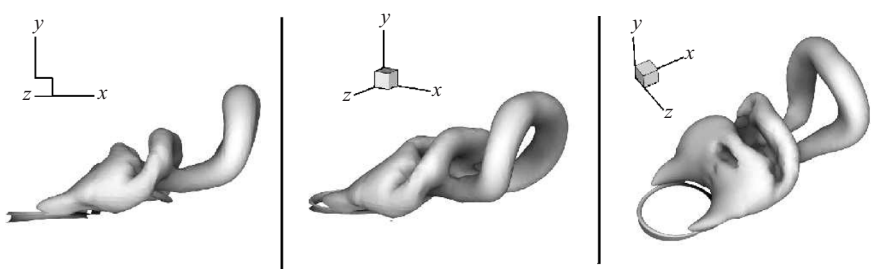

FIGURE 11. Hairpin structures are shed for $L/D = 5$ at $r = 1$. The figures correspond to $t^* = 5.0$.

structure is formed due to the roll-up on the downstream side alone. This formation of hairpin vortices is similar to that observed in the experiments of Acarlar & Smith (1987) at velocity ratios much smaller than those used in our simulation.

3.2.1. *Large L/D: hairpin vortex shedding*

For low velocity ratios and large stroke ratios, a series of hairpin vortices is shed downstream. Figure 11 shows an iso-surface of pressure for $L/D = 5$ and $r = 1.0$. Note that once a hairpin vortex is discharged, then the next hairpin starts to form. This shedding of hairpin vortices is Reynolds-number dependent. Figure 12 shows vorticity contours in the symmetry plane at different Reynolds numbers: 600, 300 and 150. The stroke ratio $L/D = 100$ so that the periodic shedding of the hairpins can be observed. Instantaneous contours of vorticity are shown at $t^* = 20$ for each of the cases. Note that for $Re = 600$, the vortices are unstable. For lower Reynolds number, periodic shedding of coherent hairpins is observed as shown. Also, the shedding frequency depends upon the Reynolds number.

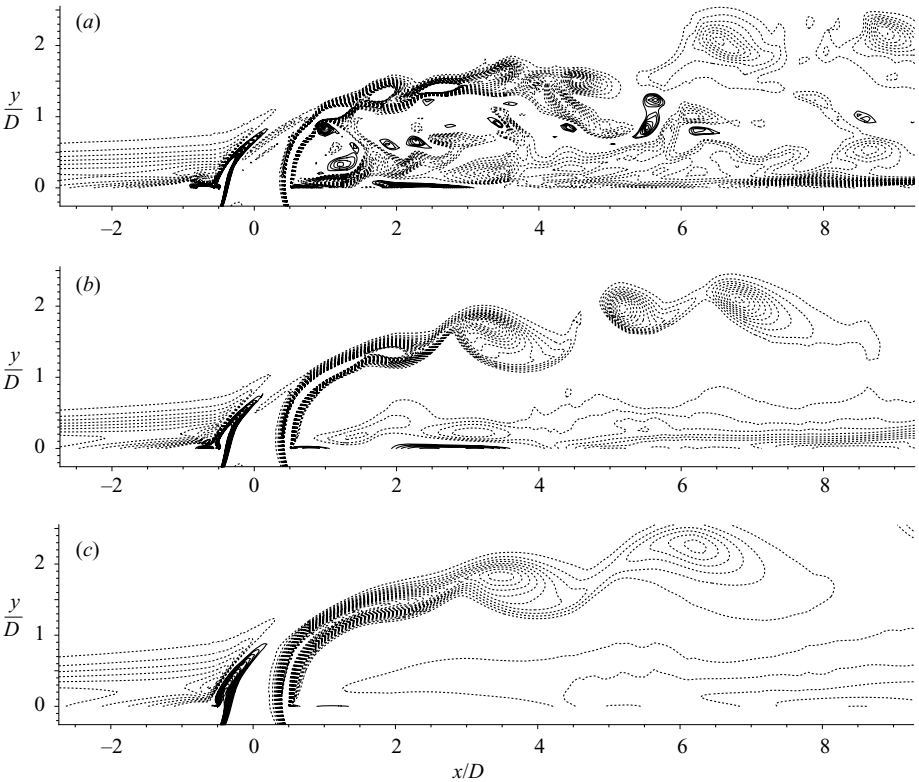

FIGURE 12. Vorticity contours in the symmetry plane at $t^* = 20$ for $r = 1.0$ and $L/D = 100$. (a) $Re = 600$, (b) $Re = 300$, (c) $Re = 150$. Note that shedding of the hairpin vortices is unstable at $Re = 600$. The shedding is very periodic for lower Reynolds number.

The evolution of hairpin vortices may be explained as follows. Figure 13 shows a hairpin structure and its image in the presence of the wall. Schematics of the hairpin cross-sections in spanwise and symmetry planes are also shown. The symmetry plane cuts the 'head' off the hairpin structure. The spanwise plane consists of its counter-rotating legs. The presence of the wall can be modelled by the image vortices as shown in the schematic. In the spanwise plane, the counter-rotating 'legs' follow the path shown as a thick-dotted line in figure 13. The legs approach each other and also move upwards due to their mutual induction and interaction with the image vortices. On the other hand, the crossflow exerts an upward Kutta–Joukowski lift force on the head of the hairpin and the image vortex induces a negative u-velocity. As a result, the head portion of the hairpin tilts as it propagates downstream and becomes normal to the crossflow direction as shown in figure 11. The hairpin structure detaches from the emerging shear layer due to the particular motion of the hairpin legs in the presence of the wall. While the hairpin detaches from the shear layer and is shed downstream, the next hairpin is formed.

These results suggests that for very low velocity ratio and low Reynolds number, a steady jet in the presence of a crossflow results in a series of hairpin structures. And if the Reynolds number is very low then the horseshoe-like vortices are shed in a periodic manner. This suggests that at very low velocity ratios, the structure of jets in crossflow is quite unlike the classical structure where the counter-rotating vortex

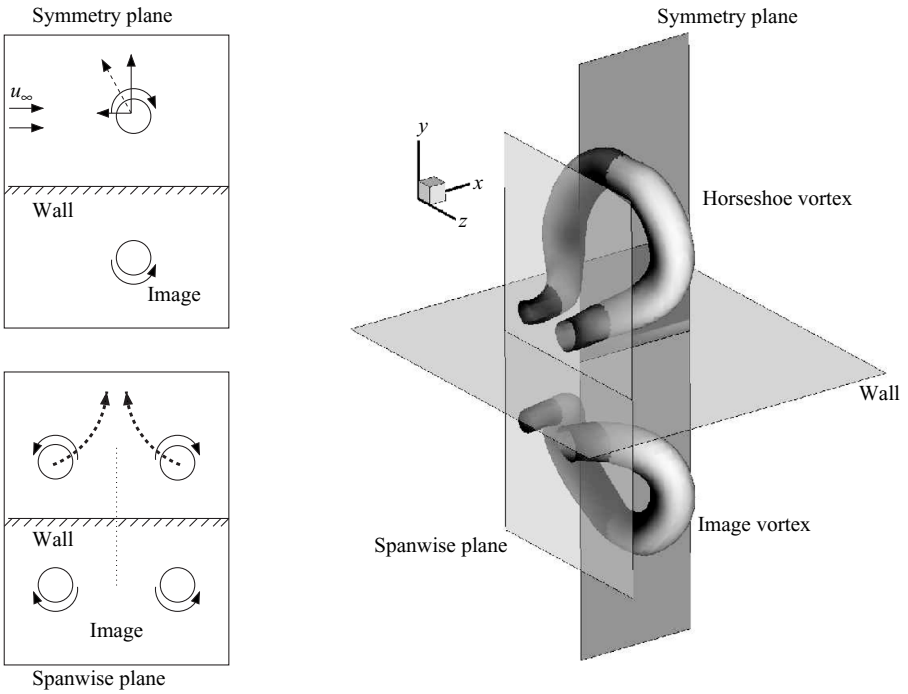

FIGURE 13. Evolution of a hairpin vortex structure in the presence of a wall. The dotted curves in the spanwise plane show the trajectory of the legs due to the wall.

pair (CVP), a stationary horseshoe vortex, wake vortices and Kelvin–Helmholtz instability vortices characterize the flow (Fric & Roshko 1994). This observation is also consistent with the experiments of Gopalan, Abraham & Katz (2004) on a turbulent jet in crossflow at $r < 2$. They report that a semi-cylindrical vortical layer forms behind the jet and suggest that this vorticity starts from the jet shear layer.

4. Mixing and entrainment characteristics

The mixing of nozzle fluid with the crossflow fluid is studied by the transport of a passive scalar. The Schmidt number Sc of the scalar is 1.0. Fluid exiting from the nozzle has scalar concentration of 1. The crossflow fluid which initially had scalar concentration of zero, mixes with the nozzle fluid to give intermediate scalar values between zero and one. When the ambient fluid is stationary, an axisymmetric vortex ring entrains the ambient fluid radially inward into the core when it forms. The entrained ambient fluid mixes with the nozzle fluid inside the core. In contrast, the trailing column is surrounded by quiescent ambient fluid and does not entrain the ambient flow. The trailing column is much less effective than a single vortex ring in entraining the ambient fluid and mixing by vortex rings in stationary fluid is optimal at a stroke ratio equal to the formation number (Sau & Mahesh 2007). The presence of crossflow changes the mixing and entrainment characteristics completely. As shown above, three different flow regimes exist depending on the velocity ratio and stroke ratio. The different entrainment mechanisms of these three flow regimes are studied below.

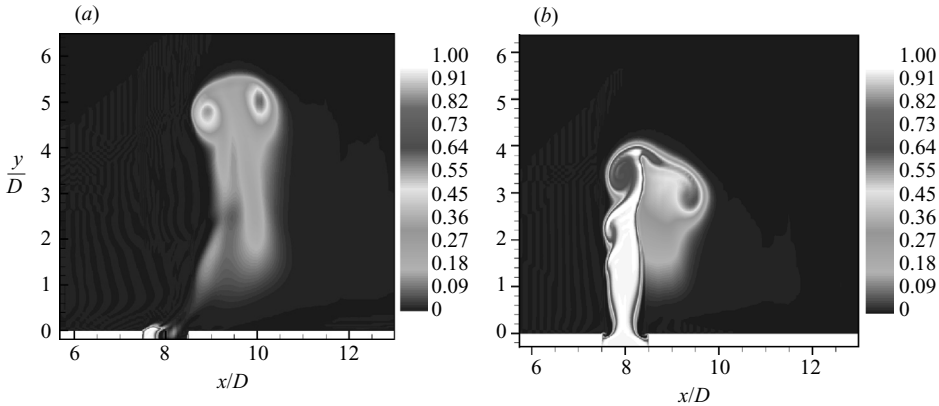

FIGURE 14. Instantaneous scalar contours on the symmetry plane for a vortex ring in crossflow with $r = 6$ and L/D of (*a*) 2 and (*b*) 6. Note the asymmetry in the scalar concentration in the case of small stroke ratio, and the enhanced downstream mixing for the case of large stroke ratio.

4.1. *Velocity ratio* > 2

Figures 14(*a*) and 14(*b*) show scalar contours in crossflow of $r = 6$ for vortex rings with stroke ratio 2 and 6 respectively. Distinctly different mixing and entrainment behaviour can be observed. For the single vortex ring shown in figure 14(*a*), the scalar mixing is similar to that in the absence of crossflow. The vortex ring entrains the ambient fluid during its formation. The entrained fluid is mixed with the nozzle fluid inside the core and some of the fluid from the boundary of the vortex ring is deposited behind the ring as the ring propagates. The crossflow introduces an asymmetry between the cores of the ring. Figure 14(*a*) suggests that the core on the upstream side is more mixed than on the downstream side of the ring. This asymmetry in scalar mixing can be attributed to the deformation of the ring as explained in § 3.1.1.

For large stroke ratios, scalar contours in figure 14(*b*) clearly show that the mixing on the downstream side is enhanced significantly. This behaviour is similar to that observed in jets in crossflow. As suggested by Muppidi & Mahesh (2008), when a jet encounters a crossflow, the jet bends and the cross-section of the jet deforms. This creates a high pressure gradient directed towards the jet on the downstream side. This pressure gradient drives the flow toward the jet and causes the jet to entrain more fluid on the downstream side rather than the upstream side. Similar flow features are observed in the present case. Figure 15 shows an iso-surface of vorticity along with three-dimensional streamlines for $L/D = 6$ and $r = 6$. The iso-surface shows the structure of the ring along with the trailing column. It is interesting to observe the streamlines and the deformation of the trailing column cross-section on the downstream side. The streamlines clearly show that crossflow fluid goes around the trailing column and is entrained from the downstream side into the trailing column and ring. This downstream entrainment is further enhanced by the low pressure in the core of the vortex ring. This behaviour is in contrast to that in the absence of crossflow where the trailing column does not significantly contribute to overall mixing.

Is there an optimal length of trailing column? For low stroke ratios (no trailing column or a very small one), enhancement due to downstream entrainment is absent. On the other hand, for very large stroke ratios, the leading ring would be far away

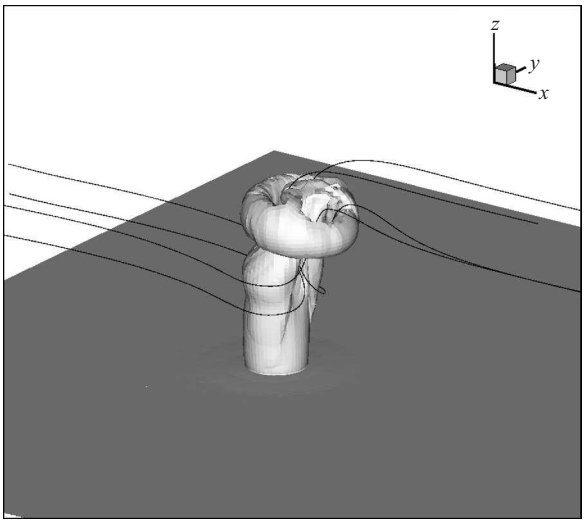

FIGURE 15. Iso-surface of vorticity along with some three-dimensional streamlines for $L/D = 6$ and $r = 6$. The streamlines show the downstream entrainment of the crossflow fluid.

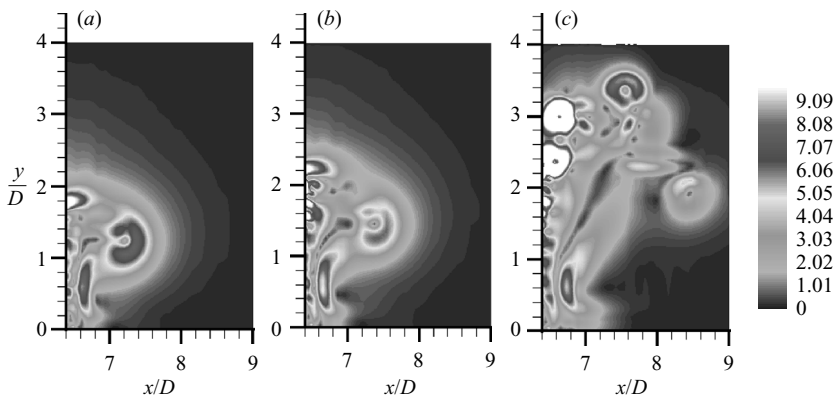

FIGURE 16. Contours of pressure gradient magnitude ($|\nabla p|$) at different times: (*a*) $t^* = 3.7$, (*b*) $t^* = 5.0$, (*c*) $t^* = 7.0$. Note that the pressure gradient magnitude around the downstream of the trailing column is maximum around $t^* = 5.0$.

from the high-pressure region downstream of the trailing column and would not contribute to enhance the downstream pressure gradient.

4.1.1. *Optimal downstream pressure gradient*

In order to obtain the optimal length of trailing column, the variation of pressure gradient magnitude with the length of the trailing column is computed for velocity ratio 3. Figure 16 plots the contours of pressure gradient magnitude ($|\nabla p|$) in the symmetry plane at different time instants. The figure shows that a high pressure gradient magnitude (denoted by $|\nabla p|_{tr}$) is created on the downstream side of the trailing column. Note that $|\nabla p|_{tr}$ increases till approximately $t^* = 5.0$, following which it decreases. So, for optimal downstream entrainment, the length of the trailing column

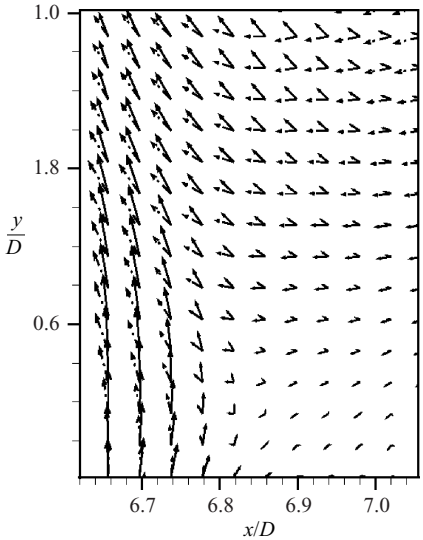

FIGURE 17. Pressure gradient vectors on the symmetry plane near the downstream pressure gradient region at two different time instants: — — —, $t^* = 3.7$; ——, $t^* = 5.0$. Note that the vectors rotate towards the right in the direction of the vortex ring core.

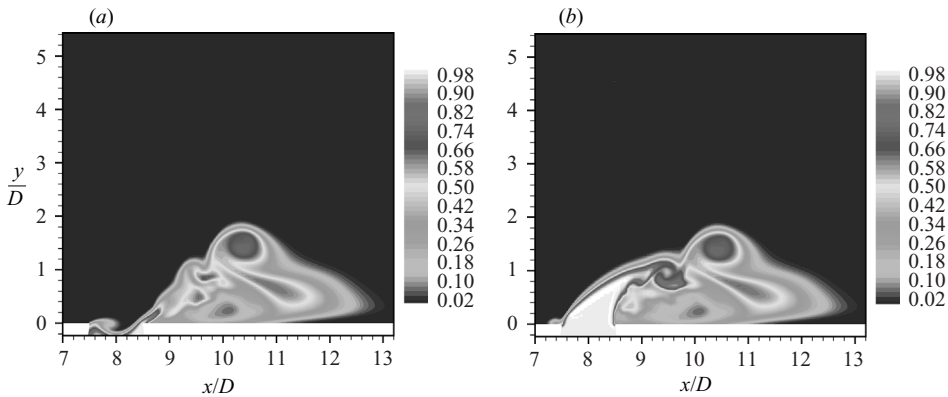

FIGURE 18. Instantaneous scalar contours on the symmetry plane for $r = 1$ and L/D of (a) 3 and (b) 5.

should be at stroke ratio equal to 5. The effect of the leading ring on the downstream pressure gradient is shown in figure 17. The downstream side of the trailing column is enlarged to show the pressure gradient vectors at two different time instants, chosen when $|\nabla p|$ is increasing. Note that the pressure gradient vectors rotate towards the right, in the direction of the leading vortex ring.

4.2. *Velocity ratio < 2*

Recall that for very low velocity ratio, a hairpin structure forms instead of a vortex ring, and that a series of hairpins is shed downstream for large stroke ratios. Figures 18(c) and 18(d) show the scalar contours in the symmetry plane for hairpin structures at $r = 1$ for stroke ratios of 3 and 5 respectively. It is immediately apparent

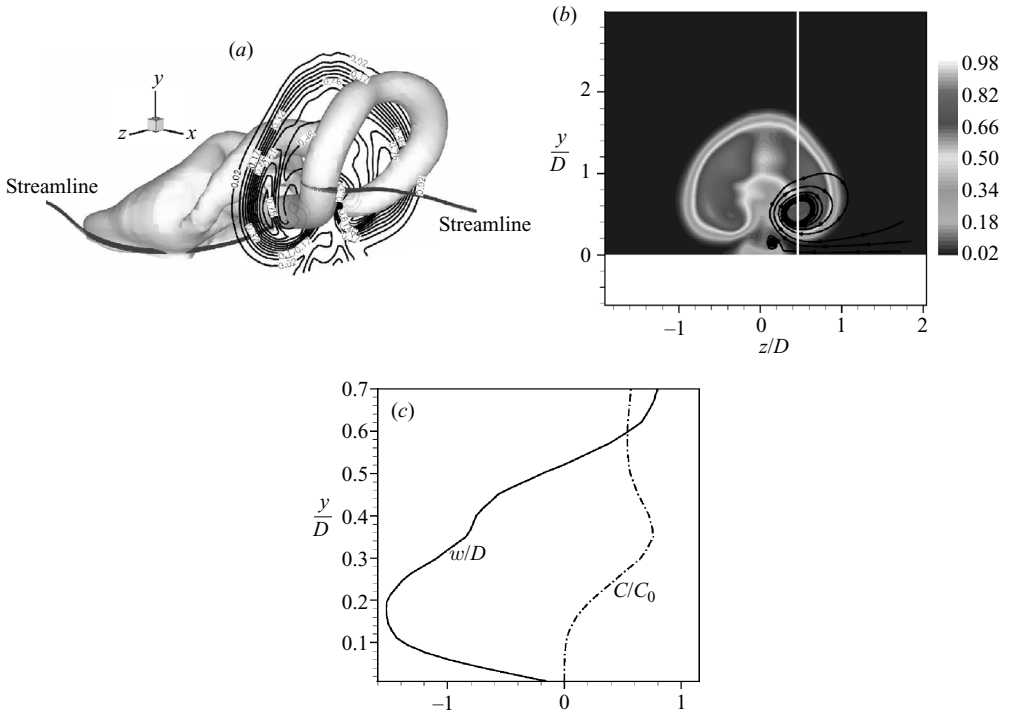

FIGURE 19. Entrainment by hairpin vortex legs. (*a*) Scalar contour lines on a spanwise cross-section of the hairpin legs at $x = 1.9$. (*b*) The corresponding scalar contours on the spanwise plane along with some in-plane streamlines. (*c*) Spanwise velocity (w/D) and scalar concentration (C/C_0) profiles along a line passing through one of the cores of the hairpin legs on the spanwise plane.

that the mixing behaviour is quite different from that observed at high velocity ratios. These differences are discussed in detail below.

4.2.1. *Entrainment by hairpin legs*

Figure 19(*a*) shows the hairpin structures for $L/D = 5$ at $r = 1$ along with scalar contour lines on a spanwise plane at $x/D = 1.9$. A streamline emanating from near the nozzle exit is also shown. Figure 19(*b*) shows scalar contours in the spanwise plane ($x/D = 1.9$) which cuts the counter-rotating legs of the hairpin, and some instantaneous streamlines around one of the hairpin-leg cores. A very low-pressure region is created at the core. The resulting pressure gradient causes the crossflow fluid around the legs to be entrained. This entrainment could also be explained as Biot-Savart induction by the vortex cores in the hairpin legs. The streamlines in figure 19(*b*) show this entrainment of crossflow fluid by the hairpin legs. To further illustrate this behaviour, w-velocity and scalar concentration profiles are plotted in figure 19(*c*) along a line passing through one of the cores of the hairpin legs on the spanwise plane at $x/D = 1.9$. The figure shows large levels of w-velocity near the vortex core close to the wall. The scalar concentration of the fluid with strong w-velocity is close to zero, indicating crossflow fluid. An interesting point to note here is that the scalar contours due to the counter-rotating hairpin legs in the spanwise plane appear similar to those of the counter-rotating vortex pair (CVP), observed in a jet in crossflow, although in the present case, a CVP does not exist.

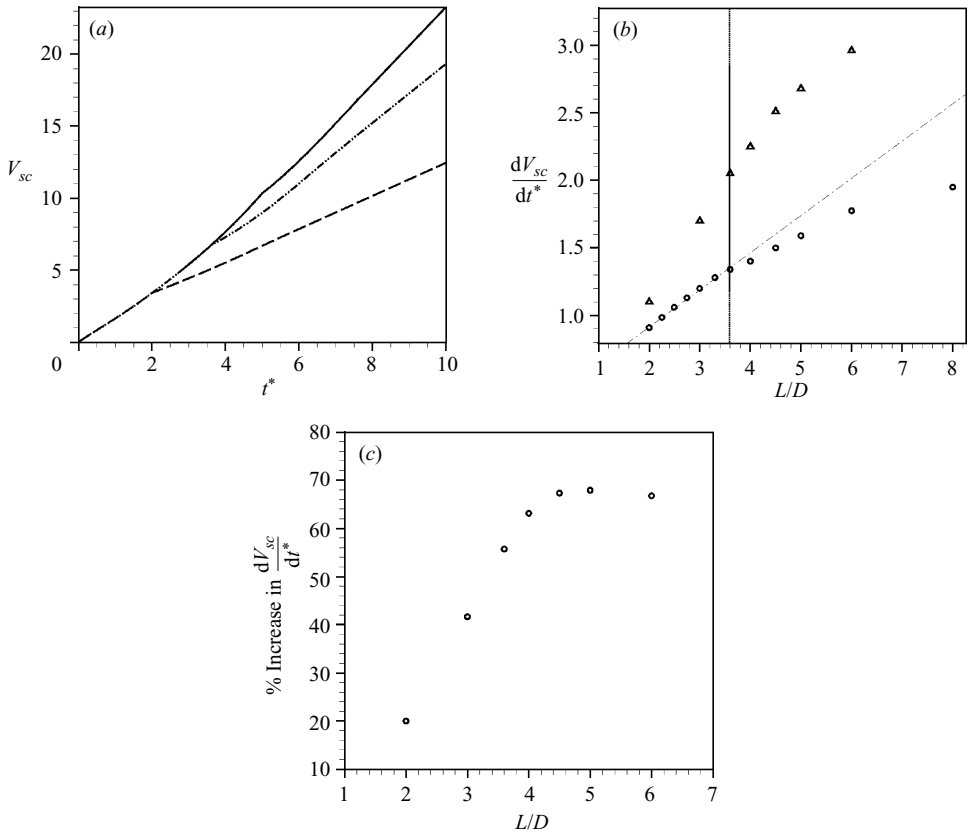

FIGURE 20. (*a*) Variation of volume of scalar-carrying fluid with time for different stroke ratios and $r = 3$: — — —, $L/D = 2.0$; —— ·· ——, $L/D = 3.6$; ———, $L/D = 5.0$. (*b*) The rate of change of scalar volume after formation against the stroke ratio for $r = 3$ (△). The results for the vortex rings in the absence of crossflow are also shown (○). The vertical line denotes the formation number. The dot-dashed line shows the linear dependence for stroke ratios less than the formation number in the absence of crossflow. (*c*) Percentage increase in the rates due to crossflow are plotted against the stroke ratio. Note that the percentage increment is maximum around $L/D = 5$.

4.3. *Rate of Mixing*

The mixing is quantified by computing the rate of change of total volume of scalar after formation. The procedure is similar to that followed by Sau & Mahesh (2007) for vortex rings without crossflow. Figure 20(*a*) shows the total volume of scalar-carrying fluid (V_{sc}) plotted against non-dimensional time (t^*) for different stroke ratios and a velocity ratio of 3. V_{sc} is computed as the sum of all volume elements which have scalar concentrations above a threshold value (set to 0.01) in the domain above the nozzle exit plane ($y/D > 0$). The slopes of these volume curves after the formation of the ring yield the rate of change of total volume of scalar-carrying fluid. The rates are shown in Figure 20(*b*) along with the results for rings without crossflow. The figure suggests that the crossflow enhances the mixing in each of the cases, but the enhancement is much higher for larger stroke ratios. This is due to the enhanced downstream entrainment by the trailing column. The percentage increase in entrainment rate for each stroke ratio is shown in figure 20(*c*). For a stroke ratio of 2, the rate of volume change increases only about 20%. The increase is about 40%

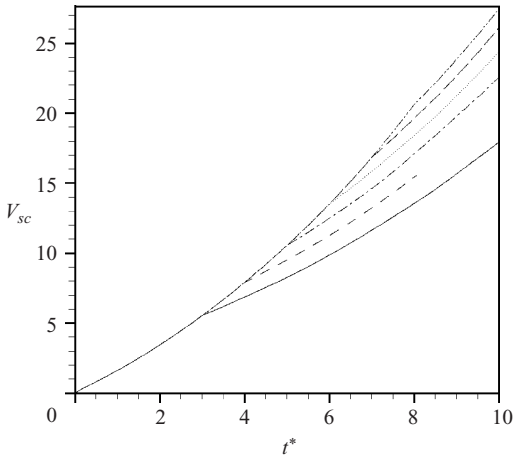

FIGURE 21. Variation of volume of scalar-carrying fluid with time for different stroke ratios and $r = 1$: ——, $L/D = 3.0$; — — —, $L/D = 4.0$; —·—, $L/D = 5.0$; ·····, $L/D = 6.0$; — — —, $L/D = 7.0$; —··—, $L/D = 8.0$. Note that the slope of the volume curve after formation is almost the same for all stroke ratios.

for stroke ratio of 3 and about 70% for stroke ratio 4.5. The percentage increase in rate appears optimal around a stroke ratio of 4.5, which is consistent with optimal downstream pressure gradient.

The behaviour for low velocity ratios is different. Figure 21 shows the total volume of scalar-carrying fluid for different stroke ratios and $r = 1$. Note that the slopes of the curves after formation are nearly equal. The rate of change of V_{sc} in this case is therefore nearly the same at all stroke ratios. This behaviour is due to the formation of hairpin structures at low velocity ratios. As shown earlier, periodic hairpin vortices are generated at all stroke ratios. Therefore this regime does not have an optimal stroke ratio which maximizes entrainment of crossflow fluid.

5. Summary: a global classification map

Vortex rings in crossflow can be classified into three different regimes with differing flow structures, mixing and entrainment characteristics. Figure 22 shows these different regimes in the space of stroke ratio (L/D) and velocity ratio (r). This 'global classification map' includes the transition curve for $r > 2$. The transition curve defines the transition from a discrete vortex ring (upstream tilting) to a vortex ring with a trailing column (downstream tilting). As the velocity ratio approaches very high values, the flow field approaches a vortex ring in stationary fluid, and consequently, the transition stroke ratio approaches the 'formation number'. Again, as the stroke ratio increases toward very large values, the flow field approaches a jet in crossflow. The regime to the right of the transition curve is characterized by enhanced downstream entrainment due to the trailing column structure, and, for a particular velocity ratio, there is an optimal length of the trailing column. For velocity ratio less than approximately 2, complete vortex ring structures do not form. This regime is characterized by the formation of hairpin-like vortex structures.

The global classification map has important implications. It categorizes the complete space of velocity ratio and stroke ratio into three different regimes. A desired flow feature can be attained by choosing the corresponding parameter from the map.

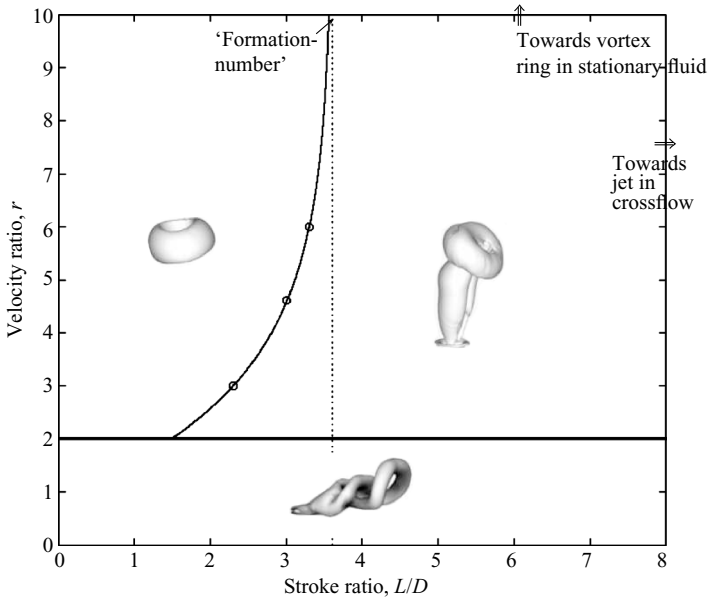

FIGURE 22. A classification map showing three regimes with different flow structure and entrainment characteristics.

Consider pulsation of the jet as a means to control jets in crossflow. A pulsed jet generates a series of vortex rings. The equivalent stroke ratio of each vortex ring can be easily derived from the pulsing parameters (e.g. Strouhal number, duty cycle, waveform). For example, the equivalent stroke ratio is the inverse of Strouhal number for a fully modulated pulsed jet with 50% duty cycle and square waveform. Thus, for a fixed crossflow, the pulsing parameters can be chosen from the map according to the desired flow structure and entrainment characteristics.

This work was supported by the Air Force Office of Scientific Research (AFOSR) under grant FA-9550-04-1-0064. Computer time was provided by the National Center for Supercomputing Applications (NCSA), Minnesota Supercomputing Institute (MSI) and the San Diego Supercomputer Center (SDSC). We thank Dr Suman Muppidi for helpful discussions.

REFERENCES

ACARLAR, M. S. & SMITH, C. R. 1987 A study of hairpin vortices in a laminar boundary layer. Part 2. Hairpin vortices generated by fluid injection. *J. Fluid Mech.* **175**, 43–83.

BLOSSEY, P., NARAYANAN, S. & BEWLEY, T. R. 2001 Dynamics and control of a jet in crossflow: direct numerical simulation and experiments. *Proc. IUTAM Symp. Turbulent Mixing Combustion* (ed. A. Pollard & S. Candel), Kluwer., pp. 45–56.

CHANG, Y. K. & VAKILI, A. D. 1995 Dynamics of vortex rings in crossflow. *Phys. Fluids* **7**, 1583–1597.

EROGLU, A. & BRIEDENTHAL, R. E. 2001 Structure, penetration and mixing of pulsed jets in crossflow. *AIAA J.* **39**, 417–423.

FRIC, T. F. & ROSHKO, A. 1994 Vortical structure in the wake of a transverse jet. *J. Fluid Mech.* **279**, 1–47.

GHARIB, M., RAMBOD, E. & SHARIFF, K. 1998 A universal time scale for vortex ring formation. *J. Fluid Mech.* **360**, 121–140.

Gopalan, S., Abraham, B. M. & Katz, J. 2004 The structure of a jet in cross flow at low velocity ratios. *Phys. Fluids* **16**, 2067–2087.

Johari, H. 2006 Scaling of fully pulsed jets in crossflow. *AIAA J.* **44**, 2719–2725.

Karagozian, A. R., Cortelezi, L. & Soldati, A. 2003 Manipulation and control of jets in crossflow. CISM Courses and Lectures No. 439, International Center for Mechanical Sciences, Springer Wien, New York.

Mahesh, K., Constantinescu, G. & Moin, P. 2004 A numerical method for large–eddy simulation in complex geometries. *J. Comput. Phys.* **197**, 215–240.

M'Closkey, R. T., King, J. M., Cortelezzi, L. & Karagozian, A. R. 2002 The actively controlled jet in crossflow. *J. Fluid Mech.* **452** 325–335.

Muppidi, S. 2006 Direct numerical simulations and modeling of jets in crossflow. PhD Thesis, University of Minnesota.

Muppidi, S. & Mahesh, K. 2008 Direct numerical simulation of passive scalar transport in transverse jets. *J. Fluid Mech.* **598**, 335–360.

Sau, R. & Mahesh, K. 2007 Passive scalar mixing in vortex rings. *J. Fluid Mech.* **582**, 449–491.

Shapiro, S. R., King, J. M., Karagozian, A. R. & M'Closkey, R. T. 2006 Optimization of controlled jets in crossflow. *AIAA J.* **44**, 1292–1298.

Ting, L. & Tung, C. 1965 Motion and decay of a vortex in a nonuniform stream. *Phys. Fluids* **8**, 1039–1051.

Wu, J. M, Vakili, A. D. & Yu, F. M. 1988 Investigation of interacting flow of nonsymmetric jets in crossflow. *AIAA J.* **26**, 940–947.